Varactor-Integrated Single-Port Antenna Array With Element-Wise Coupling Optimization for Scalable Beamforming in 6G Massive MIMO Systems

Seungwoo Bang, *Graduate Student Member, IEEE,* Jaehoon Kim, *Member, IEEE,* Jungi Jeong, *Member, IEEE,* Junhwa Oh, *Member, IEEE,* Byeongjin Kim, *Graduate Student Member, IEEE,* and Jungsuek Oh, *Senior Member, IEEE*

***Abstract*—This paper presents a high-efficiency reconfigurable antenna array architecture that utilizes varactor diodes for beam steering at 28 GHz. To enable efficient beamforming without increasing RF complexity, a single-port antenna array is designed based on standing-wave excitation. The phase tuning range is maximized through extended series capacitance, and a triangular array configuration is adopted to mitigate mutual coupling and reduce interference. An element-level coupling optimization method is further introduced to stabilize the standing wave along the array, ensuring uniform excitation across multiple elements. The proposed optimization method achieves an aperture efficiency of 67.6% and a beam scanning range of 120° in a 1×8 array simulation. Fabricated prototypes validate the approach at 28 GHz, achieving over 41.2% aperture efficiency and a beam scanning range of 100°, even under practical fabrication conditions involving manual soldering and non-ideal diode alignment. In addition, parasitic and nonlinear characteristics of the varactor diode were analyzed to assess large-signal behavior and power-handling capability, providing a more realistic evaluation of the antenna's applicability in practical massive MIMO systems. These results demonstrate the proposed antenna's suitability for scalable, high-performance beamforming in future millimeter-wave systems.**

***Index Terms*—Reconfigurable antennas, varactor diode, beam steering, aperture efficiency, standing-wave excitation, coupling optimization.**

I. Introduction

As the evolution of mobile communications progresses from 5G toward 6G, there is a growing demand for higher data throughput and support for massive user connectivity [1]–[5]. In this context, the deployment of Extreme Massive Multiple-Input Multiple-Output (E-mMIMO) systems that integrate many more antenna ports per base station has become a key research focus. As the operating frequency increases beyond the sub-6 GHz range, the smaller element aperture allows more elements to fit in the same footprint. While this allows for the potential placement of more antenna elements, practical constraints, such as the size and cost of RF front-ends and baseband circuitry, limit a one-to-one mapping between antenna elements and RF ports. Consequently, antenna arrays at millimeter-wave frequencies are typically configured in a subarray architecture, where a single RF chain drives multiple antenna elements [6]–[13]. This architecture accommodates large baseband hardware and plays a crucial role in mitigating offset mmWave path loss.

Subarray architectures offer the advantage of utilizing a larger effective aperture for a given number of RF channels compared to full-array configurations, thereby improving spatial resolution and facilitating better port-to-port isolation [14]–[17]. However, beamforming degrades along the grouping dimension, producing grating lobes and higher scan loss at wide angles. To address the beamforming limitations associated with subarray architectures, considerable research efforts have focused on incorporating tunable components directly into antenna elements to enable per-element phase control. This approach decentralizes phase shifting operation from the RF front-end to the elements using reconfigurable parts (PIN/varactor diodes or liquid crystal) [18]–[27]. As a result, independent phase adjustment can be achieved without increasing the number of RF ports. Fig. 1 illustrates the conceptual difference between conventional subarray architectures and the proposed reconfigurable system. Conventional subarrays, which typically arrange RF ports along the azimuth direction, are limited in their ability to perform beamforming in the elevation plane, thereby restricting beam coverage. In contrast, the proposed architecture adopts tunable components to enable beamforming in both azimuth and elevation, effectively expanding the coverage. For example, a liquid-crystal-based series-fed antenna reported in 2023 [18] demonstrated 60° of 3-dB scan range and achieved 30% aperture efficiency in a subarray configuration where ten elements were driven by a single RF port.

In this work, a varactor-diode-based reconfigurable subarray antenna system is proposed to address the aforementioned limitations of conventional subarray architectures. At this point, a natural question may arise regarding how the proposed design fundamentally differs from previously reported works, such as [18], which also employ tunable elements for beam steering. One might question whether the novelty lies solely in the substitution of the tunable component. In response, the

Manuscript received. This work was supported by SAMSUNG Research, Samsung Electronics Company, Ltd. (*Corresponding author: Jungsuek Oh.*)

Seungwoo Bang, Byeongjin Kim and Jungsuek Oh are with the Institute of New Media and Communications, Department of Electrical and Computer Engineering, Seoul National University, Seoul 08826, South Korea (e-mail: littlebang97@snu.ac.kr; anjelcruso@snu.ac.kr; jungsuek@snu.ac.kr).

Jaehoon Kim is with Samsung Electronics Co., Ltd, Mobile eXperience Business, Core Component Technology Team (e-mail: jxx.kim@samsung.com).

Jungi Jeong and Junhwa Oh are with Samsung Research, Seoul 06765, South Korea (e-mail: jungi.jeong@samsung.com, james33.oh@samsung.com).

authors emphasize that the proposed architecture introduces several key innovations beyond the choice of the variable element, as detailed in the following sections.

First, it is important to note that liquid crystals and diodes represent fundamentally different mechanisms for achieving phase reconfigurability in antenna systems. Liquid crystals function as dielectric tuning materials that alter the effective permittivity of the antenna's substrate, thereby affecting the radiated phase. In contrast, varactor diodes operate as lumped elements whose tunable capacitance directly influences the antenna's radiation phase. Thus, their integration with the antenna differs substantially. In liquid-crystal-based antennas, the tunable material is typically embedded within or replaces the substrate, and the phase tuning is primarily controlled by the electric field established between the radiating patch and the ground plane. As a result, the vertical substrate thickness becomes a critical design parameter. [28]–[30]. In varactor-based antennas, the diode is mounted directly on the radiator, and the phase shift is governed by the voltage-dependent capacitance between in-plane electrodes. Therefore, the horizontal geometry, especially the element length, plays a key role in determining the phase tuning range [31]. This fundamental difference implies that the design methodologies for phase-agile antennas vary significantly depending on the type of tunable component used. Hence, design methods and challenges differ between varactor- and LC-based arrays [18]. Section II of this paper elaborates on the specific design considerations and implementation strategies adopted to overcome these challenges, focusing on the varactor-loaded antenna element and its subarray configuration.

Second, this work explores a broader range of subarray configurations aimed at optimizing the aperture efficiency of varactor-integrated antenna arrays. Section III presents the design methodology and experimental validation of subarray structures that maximize aperture efficiency under standing-wave excitation. In contrast to [18], which converted a leaky-wave antenna to standing-wave excitation via an open end, this work provides a more in-depth analysis of standing-wave excitation. Based on this analysis, a generalized approach is proposed that enables high aperture efficiency regardless of the number of antenna elements in the subarray.

As outlined above, this paper presents a systematic design methodology for varactor-based subarray antennas, as detailed in Sections II and III. Section II addresses the design challenges of varactor-integrated antenna elements and their subarray integration, while Section III discusses strategies for optimizing aperture efficiency under standing-wave excitation. Section IV describes the fabrication and measurement of a prototype to experimentally validate the proposed approach. The proposed design methodology enables efficient beam steering without increasing RF complexity, making it suitable for next-generation 6G systems requiring scalable array architectures. Finally, Section V concludes the paper.

II. Design Procedure of Varactor-based Antenna

A. Unit Element Design

Fig. 2 illustrates the equivalent circuit of the proposed reconfigurable antenna incorporating a varactor diode. The

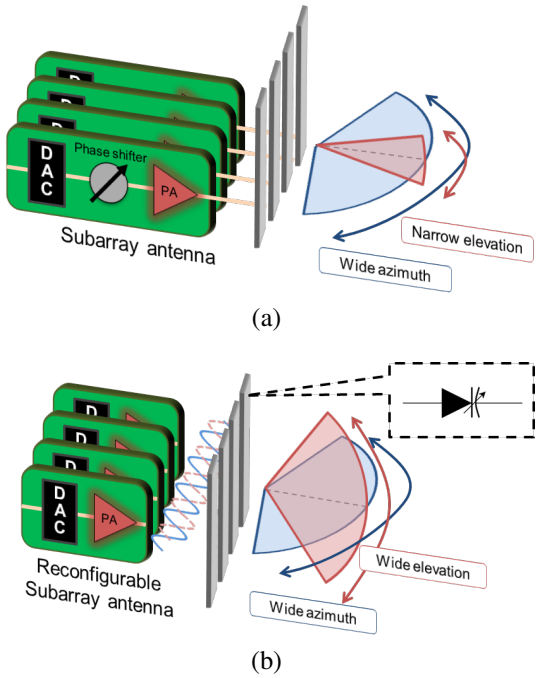

Fig. 1. Comparison between (a) a conventional subarray system and (b) the proposed reconfigurable subarray architecture.

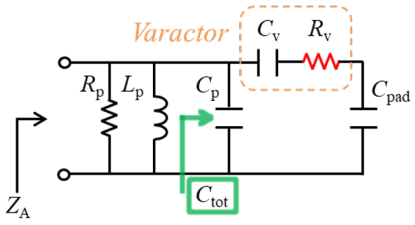

Fig. 2. Equivalent circuit of the proposed varactor-based antenna.

resonant behavior of the antenna radiator is modeled by a parallel RLC network, consisting of R_p, L_p, and C_p. A varactor diode is connected in parallel with this network, and an additional capacitance C_{pad}, representing the pad connected in series with the varactor, is also considered. The phase tuning range of the reconfigurable antenna can be analyzed by varying the varactor capacitance C_v. Therefore, it is important to identify the operating region where C_{tot} is most sensitive to C_v. The total capacitance is defined as follows:

$$C_{\mathrm{tot}} = C_p + \left(C_v \parallel C_{\mathrm{pad}}\right) \tag{1}$$

The partial derivative of C_{tot} is

$$\frac{\partial C_{\mathrm{tot}}}{\partial C_v} = \frac{C_{\mathrm{pad}}^2}{(C_v + C_{\mathrm{pad}})^2}. \tag{2}$$

Therefore, it can be observed that the sensitivity of the total capacitance, C_{tot}, to variations in the varactor capacitance is proportional to the value of C_{pad} (i.e., $\partial C_{\mathrm{tot}}/\partial C_v \propto C_{\mathrm{pad}}$). As illustrated in Fig. 3, when the phase tuning range of the resonator is evaluated with varying C_v using the equivalent circuit shown in Fig. 2, a larger tuning range is achieved when $C_{\mathrm{pad}} = 5$ pF compared to $C_{\mathrm{pad}} = 1$ pF.

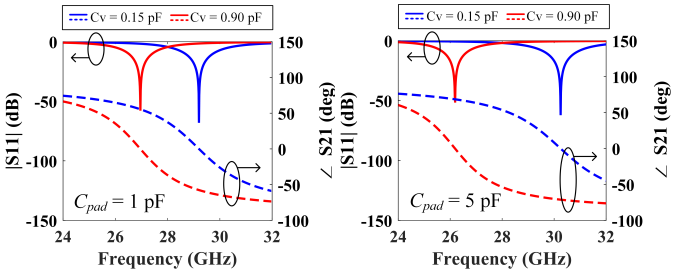

Fig. 3. Phase tuning range of the varactor-based resonator: (a) $C_{\text{pad}} = 1$ pF (b) $C_{\text{pad}} = 5$ pF.

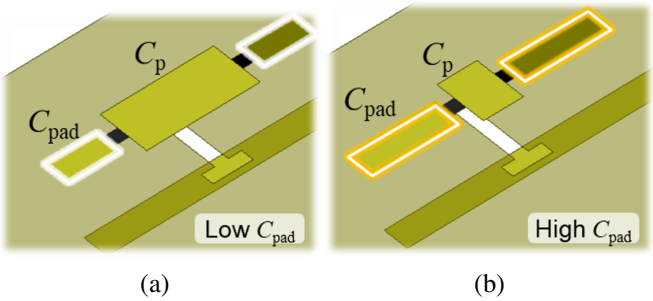

Fig. 4. Geometry for EM simulation of the varactor-based antenna: (a) Short pad length, (b) Long pad length. Black squares refer to the varactors.

To verify this behavior through electromagnetic (EM) simulation, the phase tuning range of the antenna was evaluated by varying the length of the pad connected in series with the varactor diode, as illustrated in Fig. 4. Fig. 5 presents the phase tuning results for different pad lengths. As shown in Fig. 5(b), a larger phase tuning range is obtained compared to Fig. 5(a). Thus, for a fixed resonance, pad length dominantly sets the phase-tuning range. A longer pad results in a wider phase tuning range. This agrees with the circuit model (Fig.3): a longer pad increases C_{pad}, and thus $\partial C_{\text{tot}}/\partial C_v$.

The detailed structure of the single antenna element optimized for maximizing the phase tuning range is shown in Fig. 6. A stripline feed is employed and coupled to the radiator through an aperture-coupled configuration. The radiator is connected to varactor diodes mounted at the top layer, with series-connected pads located at the end of the varactors. Bias

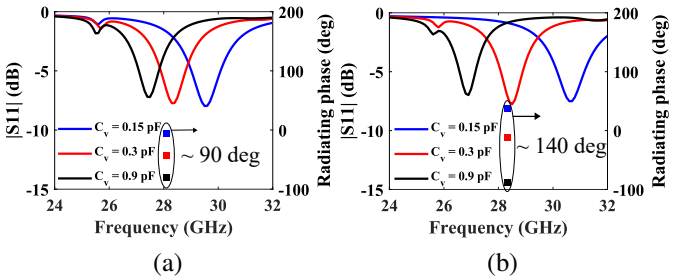

Fig. 5. Simulated phase tuning range of the antenna for different pad lengths: (a) Short pad length, (b) Long pad length. A longer pad provides a wider phase tuning range due to increased coupling capacitance.

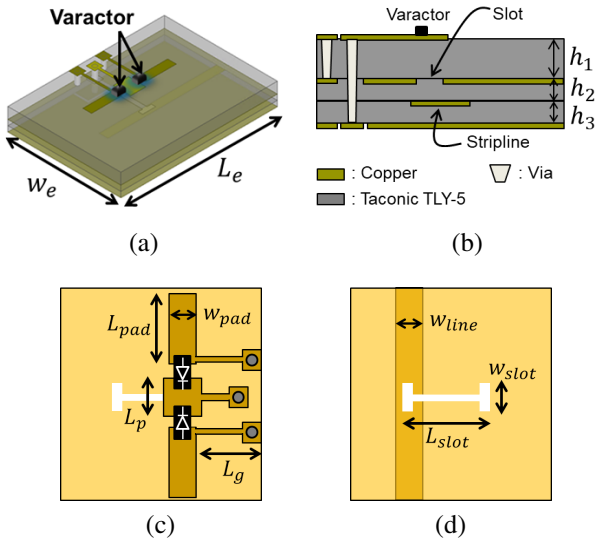

Fig. 6. Geometry of the proposed single antenna element: (a) Bird's eye view, (b) cross-sectional view, (c) 1st layer, (d) 2nd layer of the antenna element.

TABLE I
ANTENNA ELEMENT GEOMETRY (UNIT: MM)

w_e	L_e	h_1	h_2	h_3	L_{pad}
5.2	7.2	0.51	0.25	0.25	1.4
w_{pad}	L_p	L_g	w_{line}	L_{slot}	w_{slot}
0.4	0.7	1.8	0.4	1.4	0.6

lines are connected to the sides of the radiator to provide the required DC bias for tuning the varactor capacitance. Three bias lines are used. One connects to the radiator center (i.e., E-field null) to minimize RF–DC interaction; the other two terminate to DC ground via quarter-wavelength vias, appearing open at RF and isolating the RF signal. The antenna is fabricated on a Taconic TLY-5 substrate with a relative permittivity of $\varepsilon_r = 2.2$ and a loss tangent of $\tan\delta = 0.0009$, ensuring low dielectric loss at 28 GHz. The detailed geometrical parameters of the proposed antenna structure are listed in Table I. Fig. 7 presents the frequency response of the proposed varactor-integrated antenna as a function of the varactor capacitance C_v. As C_v increases from 0.15 pF to 0.9 pF, the radiation phase of the antenna exhibits a corresponding delay. The varactor diode used in this design is MAVR-000120-1411, manufactured by MACOM.

B. Triangular Array Configuration

Maximizing element-level phase range requires a longer pad connected to the varactor diode, which complicates array implementation. However, this approach introduces critical challenges when applied to array configurations. In series-fed arrays, the spacing between elements must be approximately half of the guided wavelength to suppress grating lobes and achieve high radiation efficiency [18]. As the pad length increases, the total length of each radiator approaches half of the guided wavelength. This leads to two major issues: (1)

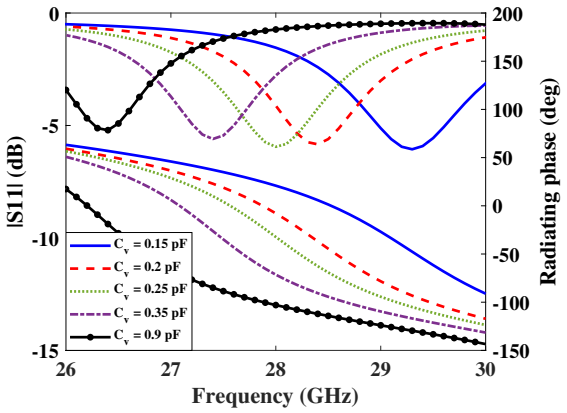

Fig. 7. Simulated frequency responses of the varactor-based single antenna element for different capacitance C_v.

physical overlap between adjacent elements, making the array difficult or impossible to fabricate; and (2) excessively close spacing that increases mutual coupling, thereby degrading the array's beamforming performance. Fig. 8(a) illustrates the configuration where antenna elements are arranged in a linear array. As shown, the lateral dimension of each antenna is comparable to the element spacing, resulting in extremely narrow gaps between adjacent elements. Consequently, when each element is individually excited through its slot port in simulation, significant coupling is observed. Even when only a single element is excited, electromagnetic fields are induced in neighboring elements. This mutual coupling effect negatively affects the overall array performance [see dashed lines in Fig. 8(d)].

To address this issue, a triangular array configuration is proposed in this work. Fig. 8(b) shows the configuration where antenna elements are arranged in a triangular array. Unlike conventional linear arrangements, antenna elements are placed in a zigzag pattern. This design offers two key advantages. First, adjacent elements are placed on different axes, preventing physical overlap even when the element length, including the pad, exceeds the lateral element spacing. Second, the capacitive coupling between adjacent pads is significantly reduced, mitigating performance degradation due to mutual interference. The effectiveness of the triangular configuration is demonstrated through EM simulations. As shown in Fig. 8(b), the mutual coupling is reduced compared to the linear array. Fig. 8(c) further illustrates improved isolation between adjacent ports at 28 GHz. As a result, the triangular array achieves a significantly higher gain of 9.5 dBi compared to 2.7 dBi for the linear array, clearly demonstrating its superior aperture efficiency (i.e., 50.1% and 10.3%, respectively), as presented in Fig. 8(d).

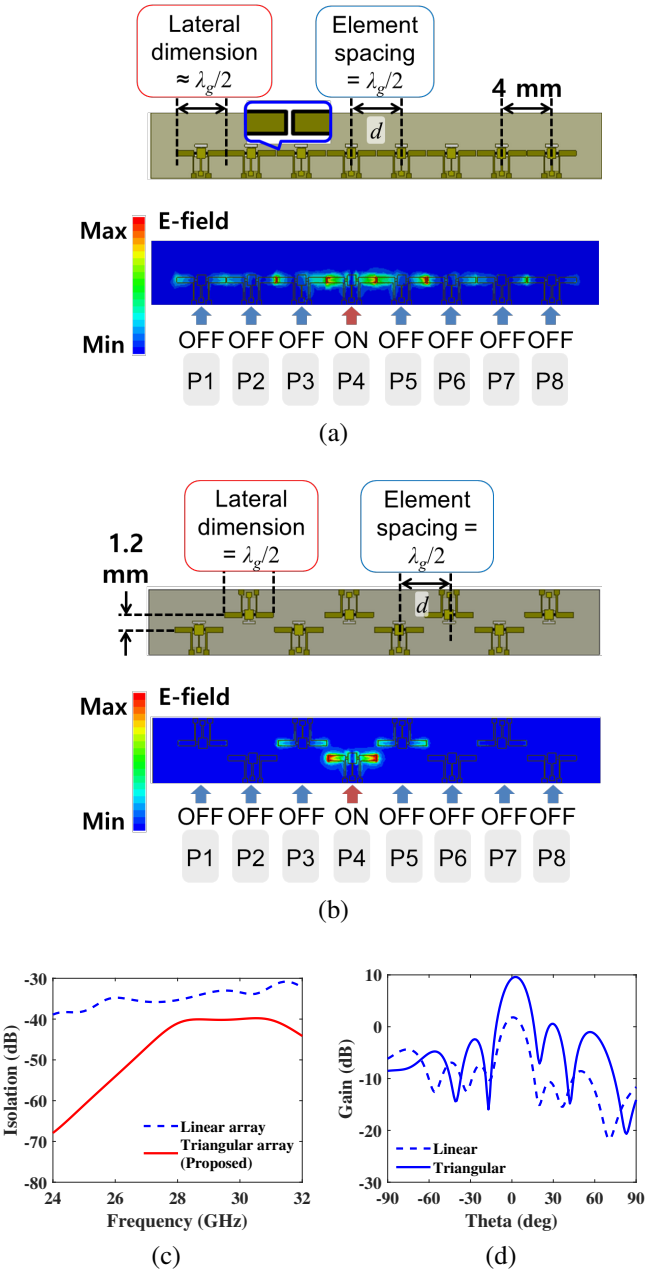

Fig. 8. E-field distribution of the varactor-based antenna array: (a) Linear array, (b) triangular array. (c) Isolation between Port 4 and Port 5 (i.e., P4 and P5), and (d) radiation pattern. All results are compared between the linear and triangular array configurations.

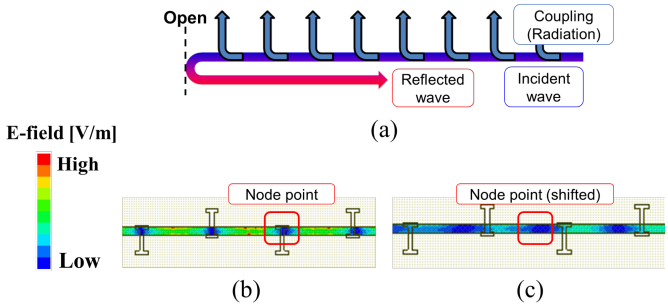

Fig. 9. (a) Illustration of the standing wave excitation and E-field distribution at 28 GHz: (b) $T = 0$, (c) $T = \pi/4$, where T is the period.

III. Coupling Optimization for Standing-Wave Stabilization in Single-Port Antenna Arrays

A. Optimization: The Number of Elements

Once a sufficient phase tuning range is secured at the element level, accurate beamforming requires several elements

per RF chain. However, in conventional reconfigurable antennas using tunable components, aperture efficiency tends to degrade as the number of elements increases. In conventional standing-wave-based array antenna design, it is commonly assumed that a uniform standing wave is established along the array, as illustrated in Fig. 9(a). Under this assumption, the incident wave propagates from the RF port to the open-ended termination and is reflected back, creating a uniform standing-wave distribution that is identical across all antenna elements. However, this assumption does not hold in practice. As the incident wave travels along the feed line and encounters each element, a portion of the energy is radiated into free space. This causes an imbalance between the amplitudes of the incident and reflected waves. In an ideal standing wave, these amplitudes are equal, resulting in fixed node points (i.e., electric field nulls). But in practice, due to the radiation via elements, the amplitude imbalance causes the node positions to become unstable, ultimately degrading the array efficiency. Fig. 9(b) and 9(c) show the time-varying electric field distribution of an 8-element array. The movement of the standing wave nodes over time can be clearly observed, indicating instability in the field distribution.

A simple mitigation is to reduce the elements per RF chain, which helps balance incident and reflected amplitudes. Fig. 10(a) shows the electric field distribution along the transmission line of a 1×4 antenna array. Compared to the 1×8 configuration, the reduced number of elements results in a more stable standing-wave pattern, with less movement in the node positions. This effect is also evident in quantitative analysis. As shown in Fig. 10(b), the aperture efficiency increases from 50.1% to 64.3% when the number of elements per RF chain is reduced from 8 to 4. In addition, Fig. 10(c) confirms that beamforming performance remains robust even with 4 elements (i.e., beam scanning range of 120°).

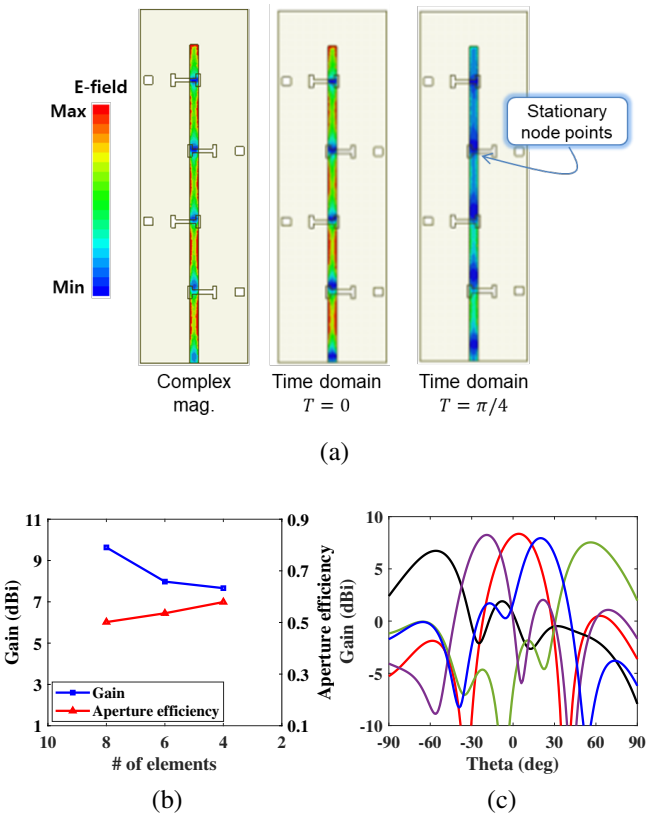

Fig. 10. (a) E-field distribution of 1×4 array configuration. (b) Aperture efficiency versus the number of antenna elements. (c) Simulated radiation patterns of 1×4 array configuration.

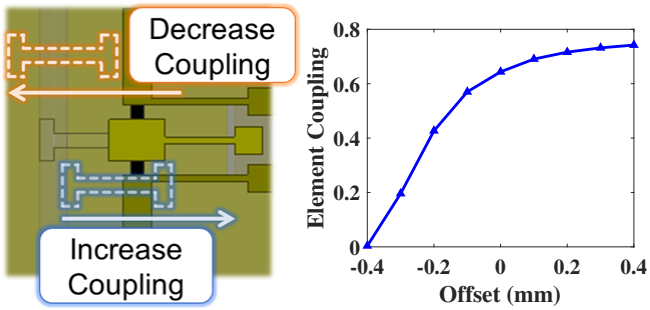

Fig. 11. (a) Closer slot placement results in stronger coupling, while increased separation leads to reduced coupling. (b) Simulated coupling coefficient with respect to the slot position.

B. Optimization: Element Coupling

However, the aforementioned approach has a fundamental limitation: the number of antenna elements per RF chain is inherently restricted. In practical subarray implementations, where a limited number of RF chains must drive a large antenna aperture, this constraint becomes a major bottleneck. Therefore, an optimization technique is required to maximize aperture efficiency regardless of the number of connected elements. To address this limitation, this work proposes a method to independently control the coupling between the antenna element and the transmission line at the element level. By adjusting the amount of radiated energy from each element, the amplitude balance between the incident and reflected waves can be maintained across the array. This coupling-based control enables stable standing-wave formation, even when a large number of elements are connected to a single RF chain. Coupling is tuned mainly by the slot position between the line and radiator. Fig. 11 presents the coupling coefficient as a function of the slot position. As the slot moves closer to the radiator, the coupled energy increases; conversely, the coupling decreases as the slot moves farther away.

To determine the optimal coupling coefficients for standing-wave stabilization, the electric field distribution along the array was first captured, as shown in Fig. 12(a). The deviation of the electric field magnitude at each element location from the array-wide average was used as a metric. As illustrated in Fig. 12(b), elements exhibiting large deviations were adjusted by modifying their individual coupling coefficients. This process was iteratively repeated to minimize the variation of induced field magnitude across the elements. Due to mutual coupling between elements, multiple iterations were required to reach a stable field distribution. Fig. 13 shows the geometry of the 1×8 array antenna after coupling optimization, along with the resulting gain improvement. Full-wave simulations confirm that the antenna gain is improved by approximately

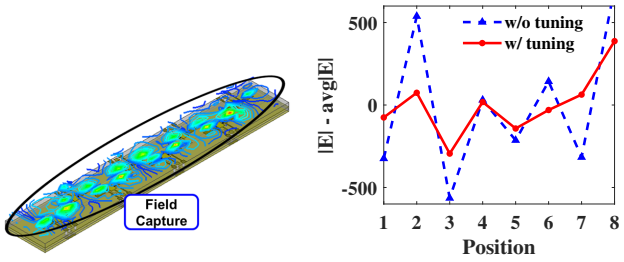

(a) (b)

Fig. 12. (a) Extracted E-field distribution along the array to identify deviation from the average at each element location. (b) Iterative adjustment of coupling coefficients to equalize E-field amplitude across all elements and stabilize the standing wave pattern.

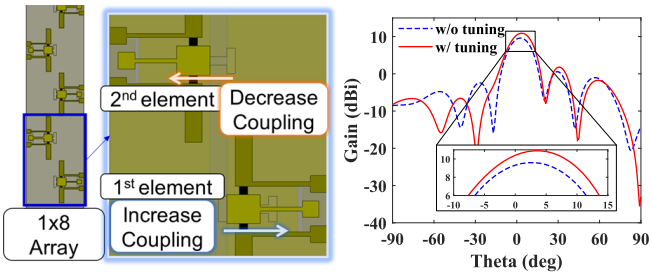

(a) (b)

Fig. 13. (a) Geometry of the 1×8 antenna array with element-wise coupling optimization. (b) Simulated realized gain improvement due to optimized coupling.

1.3 dB. As a result, the aperture efficiency increases from 50.1% to 67.6%.

To verify that the proposed coupling optimization method remains effective regardless of the number of elements, the 1×8 array was extended to a 1×12 configuration. Full-wave simulations were conducted to evaluate the antenna performance. Without coupling optimization, as shown in Fig. 14(a), the beamwidth becomes narrower due to the increased aperture. However, the excitation of a non-uniform standing wave prevents further gain improvement. As a result, the aperture efficiency decreases from 50.1% to 33.8%. In contrast, when the proposed coupling optimization method is applied, the 1×12 array achieves an aperture efficiency of 61%, as shown in Fig. 14(b). This performance surpasses that of the unoptimized 1×8 array, demonstrating that the method remains effective even as the number of elements increases.

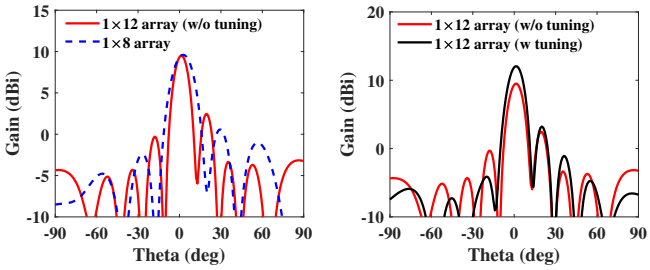

(a) (b)

Fig. 14. Comparison of radiation performance in a 1×12 array configuration: (a) Without coupling optimization, (b) with coupling optimization.

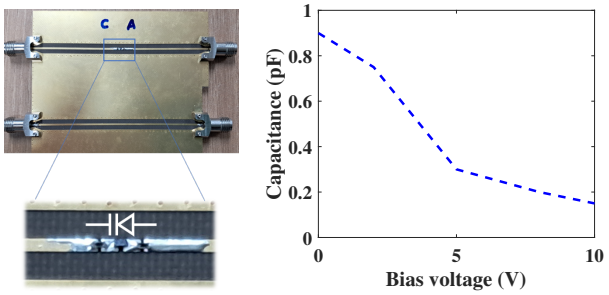

(a) (b)

Fig. 15. (a) Measurement setup and test structure for extracting the capacitance of the varactor diode at 28 GHz. (b) Extracted capacitance with respect to bias voltage.

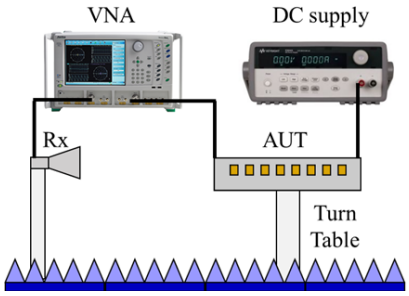

(a)

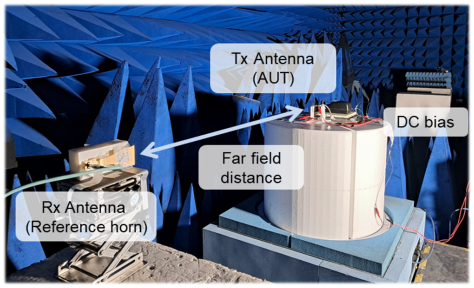

(b)

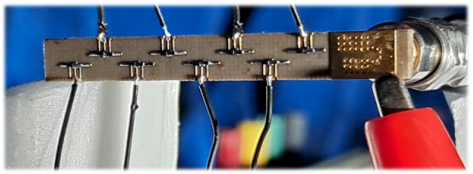

(c)

Fig. 16. (a) Schemetic of the reconfigurable antenna measurement setup, (b) photograph of the proposed antenna array, and (c) picture of the antenna and DC bias cables.

IV. Measurement and Analysis

A. Fabrication and Radiation Measurement

Prior to antenna fabrication, the capacitance characteristics of the selected varactor diode were extracted at 28 GHz.

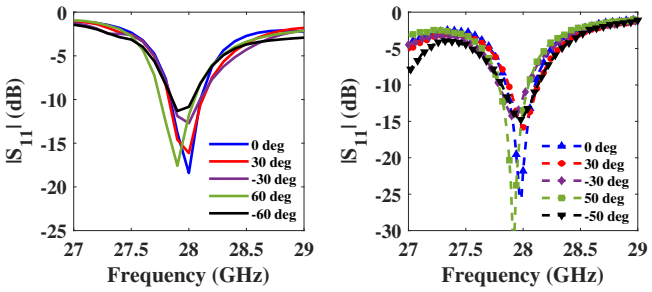

Fig. 17. Reflection coefficient of the proposed antenna array: (a) Simulation, (b) measurement.

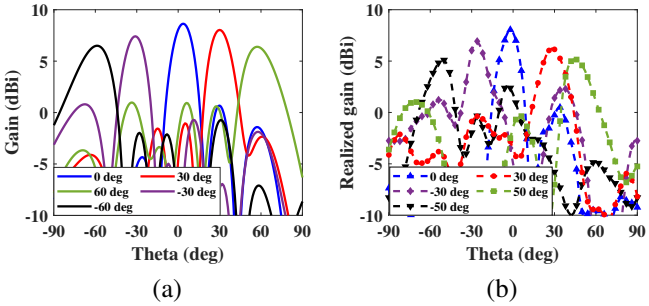

Fig. 19. Beamforming patterns of the antenna array across multiple tuning states: (a) Simulation, (b) measurement.

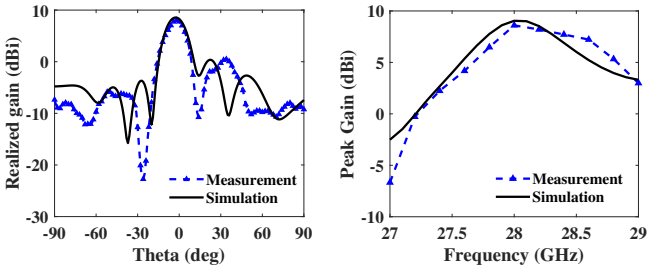

Fig. 18. (a) Simulated and measured boresight radiation patterns at 28 GHz, and (b) gain versus frequency.

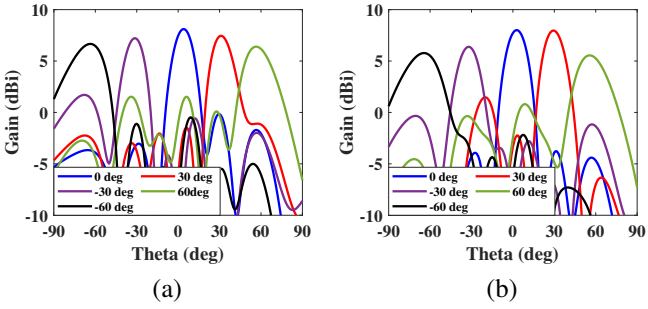

Fig. 20. Beamforming patterns of the antenna array across multiple frequencies: (a) Lower band (27.8 GHz), (b) Upper band (28.6 GHz).

Fig. 15(a) shows the measurement setup and the circuit configuration used for the extraction [32], [33]. The extracted capacitance as a function of the bias voltage is plotted in Fig. 15(b), confirming good agreement with the datasheet. The capacitance varies from approximately 0.15 pF to 0.9 pF over the measured voltage range.

Fig. 16 shows the measurement setup used to characterize the antenna, while Fig. 16(c) depicts the fabricated prototype of a 1×8 antenna array. Beamforming control voltages were supplied via DC bias cables. The reconfigurable antenna was mounted on a motorized turntable for radiation pattern measurements (i.e., Tx antenna in the Fig. 16). On the other side, a directional horn antenna is mounted at a far-field distance from the Tx antenna (i.e., Rx antenna in the Fig. 16). S-parameter was measured using a vector network analyzer (VNA), connected via 2.92 mm coaxial cables. Fig. 17 presents both the simulated and measured reflection coefficients of the antenna across various beamforming states. The simulation results confirm that the antenna maintains an $S_{11} < -10$ dB at 28 GHz for all biasing conditions. The measured results also exhibit excellent agreement with the simulations, validating consistent impedance matching across all tuning states.

Fig. 18 shows the measured boresight radiation pattern and gain-versus-frequency response of the antenna based on the setup in Fig. 16(a). While the simulated boresight gain of the antenna array reaches 10.9 dBi (corresponding to an aperture efficiency of 67.6%), the measured gain is approximately 8.6 dBi, which corresponds to an aperture efficiency of 41.2%. This discrepancy is attributed to practical losses introduced during fabrication, particularly the manual soldering of diodes directly onto the radiating structure at 28 GHz and the imperfect alignment of surface-mounted components. To reflect these effects, the series resistance of the varactor diode, which is specified as 1 Ω in the datasheet, was adjusted to 4 Ω in the simulation. With this correction, the simulated gain closely aligns with the measured result, as shown in Fig. 18. The measured gain, beamwidth, and frequency response exhibit strong agreement with the simulation results. Furthermore, Fig. 19 presents both the simulated and measured beamforming patterns of the antenna array. While the simulation shows a scanning range of 120°, the measured range is slightly reduced to 100° due to the aforementioned soldering loss and diode misalignment.

Finally, Fig. 20 presents the beamforming performance of the proposed antenna at other frequencies within the operating band. The bias voltages applied to the varactors are identical to those used for the 28 GHz beamforming states. The results confirm that the proposed antenna maintains stable beam steering without additional tuning, indicating that it can reliably transmit and receive wireless communication signals without distortion across the target band.

B. Analysis: Parasitic Effects

The parasitic components associated with the varactor diode primarily include the series resistance stemming from its intrinsic loss and the additional series inductance introduced by the packaging structure. In addition to the intrinsic semiconductor loss of the varactor itself, additional loss may also

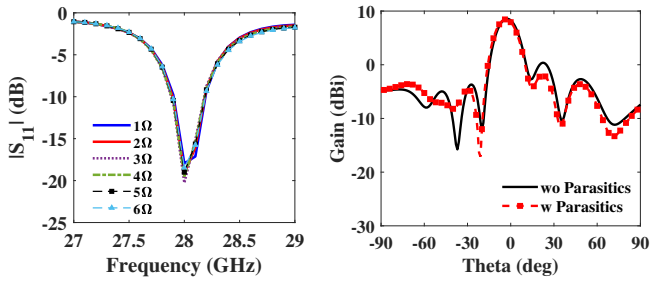

(a) (b)

Fig. 21. (a) Input impedance of the 1×8 array for different varactor series resistances. (b) Radiation patterns with and without the package-induced series inductance.

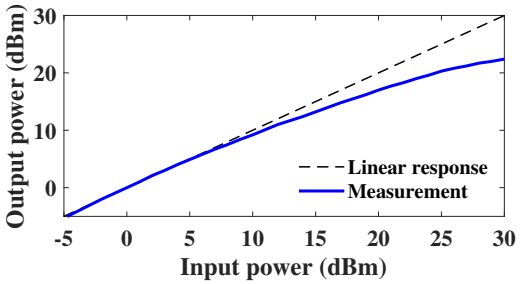

Fig. 22. Output power compression of the single varactor diode.

arise from the solder used during assembly and from misalignment of the diode during the manual mounting process.

To quantify the impact of this loss on the performance of the varactor-based antenna, full-wave simulations were conducted in HFSS by sweeping the varactor's series resistance from 1 Ω to 6 Ω. As the series resistance increased, the aperture efficiency of the proposed antenna decreased from 67.6% to 31.9%, corresponding to approximately a 3.1-dB reduction in realized gain. However, the increase in series resistance has only a minor effect on the impedance matching of the antenna. Fig. 21(a) shows the input impedance of the 1×8 array as the varactor resistance is varied. This behavior occurs because the magnitude of the varactor's series resistance is sufficiently small compared to the overall input impedance of the array, making its variation negligible in the matching response. Therefore, if automated soldering or alignment-controlled assembly is used in future prototypes, the parasitic resistance can be maintained below the 4 Ω level observed in the manual soldering process, enabling robust and high-efficiency antenna performance without impedance fluctuation.

Several studies have also investigated the series inductance introduced by the packaging of varactor diodes at millimeter-wave frequencies [34], [35]. Reported values indicate that the package inductance is on the order of 0.1 nH and 0.08 nH, respectively. Full-wave simulations performed in HFSS confirm that this level of parasitic inductance has a negligible impact on the characteristics of the proposed antenna. Fig. 21(b) compares the radiation patterns with and without the inclusion of the parasitic inductance, and no meaningful discrepancy is observed. This observation is further supported by the consistency between the simulated and measured results shown in Figs. 17 and 18, both of which were obtained without explicitly modeling the series inductance.

However, the influence of package-induced inductance becomes increasingly significant as the operating frequency increases. Therefore, for antenna designs intended for higher-frequency bands, proper modeling and compensation of the parasitic inductance will be essential to ensure accurate prediction and reliable performance.

C. Analysis: Nonlinearity

In reconfigurable-element-based antenna systems, the tunable device effectively replaces the phase shifter used in conventional phased array architectures [36], [37]. Because the varactor is directly connected to the radiator and positioned after the power amplifier in the transmit path, the device is exposed to large-signal excitation. Therefore, an analysis of the varactor's nonlinear behavior under high-power conditions is required to ensure stable performance and prevent distortion. Fig. 22 presents the output power compression measurement of a single varactor diode integrated with the proposed antenna structure. The results indicate that the varactor exhibits a 1-dB output compression point (P1dB) of approximately 12 dBm at 28 GHz.

Although the single varactor exhibits a P1dB of 12 dBm, this value does not directly represent the power-handling capability of the full array. In the proposed antenna, two varactor diodes are integrated into each element, and extending the design to a 1×8 array results in a total of 16 varactors sharing the input power across the array. Consequently, the overall power-handling level increases proportionally, yielding an estimated capability of approximately 24 dBm. Furthermore, as the number of array elements increases, the use of the proposed element-level coupling optimization helps maintain aperture efficiency while simultaneously enabling higher power-handling capability. This demonstrates that the proposed antenna design can expand in both efficiency and linearity performance.

D. Comparison

Table II provides a comparative summary of reported reconfigurable antenna arrays, including the proposed varactor-based design. Both this work and [18], which employ standing-wave excitation, demonstrate higher aperture efficiency than conventional leaky-wave-based architectures. Furthermore, the liquid-crystal-based antenna in [18] and the proposed varactor-based design differ significantly in beam-switching speed. While LC-based antennas exhibit switching times on the order of 1.6 s at millimeter-wave frequencies, diodes typically operate with nanosecond-level switching speed, making the proposed approach more suitable for real-time beamforming in massive MIMO systems [25]. In particular, the proposed design achieves further performance gains through triangular array structuring and element-level coupling optimization,

TABLE II
COMPARISON OF RECONFIGURABLE ANTENNA ARRAYS

Ref.	f_0 (GHz)	Reconfig. Component	Bias Circuit Design	3 dB Scan Range (deg)	Array Gain (dBi)	Aperture Eff. (%)	Large Signal Analysis
[18]	28	LC	Single Line	60	12.1	30	No
[20]	29	PIN	Radial Stub+Via	70	16.5	7.4	No
[21]	30	PIN	Radial Stub+Via	100	13	15	No
[22]	10	Varactor	Single Line+Via	140	10	12.6	No
[23]	12	Varactor	Capacitor+Resistor+Via	72	6.2	4.2	No
This Work	28	Varactor	Single line + Short Stub	120 (sim) 100 (meas)	10.9 (sim) 8.61 (meas)	67.6 (sim) 41.2 (meas)	Yes

enabling enhanced efficiency in densely packed array configurations.

In addition, the proposed antenna offers lower implementation complexity than many previously reported reconfigurable arrays. Unlike designs that require radial stubs or additional lumped components such as chip capacitors and resistors, the biasing network in the proposed architecture is realized solely using a single transmission line and a short stub. Moreover, unlike prior works that evaluate reconfigurable antennas solely under small-signal conditions, the proposed array is analyzed under large-signal excitation to account for the nonlinear behavior of the tunable devices. By characterizing power compression and assessing the impact of varactor nonlinearity on beamforming performance, this work provides a more practical and system-oriented solution that can be directly applied to MIMO transceivers.

V. CONCLUSION

This paper presented a high-efficiency reconfigurable antenna array architecture that utilizes varactor diodes and standing-wave excitation to achieve scalable beam steering at 28 GHz. To overcome the limitations of conventional series-fed arrays, a triangular array configuration was proposed to minimize coupling and interference. Additionally, a coupling optimization technique was introduced to stabilize the standing wave, ensuring uniform excitation across all antenna elements.

The proposed techniques were validated through both full-wave simulations and measurements. A 1×8 prototype achieved a simulated aperture efficiency of 67.6% and a beam scanning range of 120°. The fabricated antenna, despite manual soldering losses and diode misalignment, maintained a measured aperture efficiency of 41.2% and a beam scanning range of 100°. Furthermore, when extended to a 1×12 array, the optimized design outperformed the unoptimized version, proving the scalability and effectiveness of the proposed methods. In addition, the nonlinear behavior of the varactor under large-signal excitation was analyzed, enabling a more realistic assessment of power handling and demonstrating practical applicability to 6G massive MIMO systems. These results confirm that the proposed architecture is a promising solution for future millimeter-wave systems requiring high-efficiency, low-complexity beamforming.

REFERENCES

[1] Z. Wang, *et al.*, "A tutorial on extremely large-scale MIMO for 6G: Fundamentals, signal processing, and applications," *IEEE Communications Surveys & Tutorials*, vol. 26, no. 3, pp. 1560–1605, 2024.

[2] H. Yang, *et al.*, "Beyond limitations of 5G with RIS: Field trial in a commercial network, recent advances, and future directions," *IEEE Communications Magazine*, vol. 62, no. 10, pp. 132–138, 2023.

[3] H. Yang, *et al.*, "6G channel measurement in urban, dense urban scenario and massive ray-tracing-based coverage analysis at 7.5 GHz," in *ICC 2025-IEEE International Conference on Communications*. IEEE, 2025, pp. 3309–3314.

[4] W. Hong, *et al.*, "The role of millimeter-wave technologies in 5G/6G wireless communications," *IEEE Journal of Microwaves*, vol. 1, no. 1, pp. 101–122, 2021.

[5] E. Shi, *et al.*, "RIS-aided cell-free massive MIMO systems for 6G: Fundamentals, system design, and applications," *Proceedings of the IEEE*, vol. 112, no. 4, pp. 331–364, 2024.

[6] B. Kim, S. Bang, S. Yun, H. Kim, and J. Oh, "Broadband holographic mode synthesis between adjacent resonances for a low-profile thin-microstrip antenna-fed metasurface," *IEEE Transactions on Antennas and Propagation*, vol. 73, no. 11, pp. 9577–9582, 2025.

[7] S. Bang, T. Yoon, B. Kim, J. Oh, H. Kim, and J. Oh, "Extremely miniaturized free-space measurement system for RF metamaterial composite based on beam focusing transmitarray," *IEEE Antennas and Wireless Propagation Letters*, vol. 23, no. 6, pp. 1705–1709, 2024.

[8] J. Oh, H. Kim, S. Kim, J. Choi, J. Ha, and J. Oh, "M-shaped under-bridge feeding method for a low-profile dual-band dual-polarized antenna-on-package in the 6G upper-mid band," *IEEE Antennas and Wireless Propagation Letters*, vol. 24, no. 9, pp. 3164–3168, 2025.

[9] B. Kim, S. Bang, S. Kim, D. Kwon, S. Kim, and J. Oh, "Locally optimal periods in periodic optically transparent two-metal-layered refractive metasurfaces for outdoor-to-indoor communication," *IEEE Antennas and Wireless Propagation Letters*, vol. 24, no. 5, pp. 1253–1257, 2025.

[10] T. T. Nguyen, D. H. Kim, J. H. Choi, and C. W. Jung, "Circularly polarized series array and MIMO application for sub-millimeter wave/terahertz band," *Journal of Electromagnetic Engineering and Science*, vol. 24, no. 3, pp. 294–304, 2024.

[11] J. Heo, B. Kim, M. Kang, H. Kim, Y. Lee, and J. Oh, "Tetraplexing dual-broadband/dual-polarized antenna for 5G/6G millimeter-wave systems," *IEEE Transactions on Antennas and Propagation*, 2025.

[12] Z. Y. Z. T. G. A. W. H. Zheng Xuemei, Zhao Ziwei, "A low-coupling broadband mimo array antenna design for ku-band based on metamaterials," *Journal of Electromagnetic Engineering and Science*, vol. 24, no. 6, pp. 666–673, 2024.

[13] J. Oh, "Millimeter-wave short-focus thin lens employing disparate filter arrays," *IEEE Antennas and Wireless Propagation Letters*, vol. 15, pp. 1446–1449, 2015.

[14] Y. Gao and T. Kaiser, "Antenna selection in massive MIMO systems: Full-array selection or subarray selection?" in *2016 IEEE sensor array and multichannel signal processing workshop (SAM)*. IEEE, 2016, pp. 1–5.

[15] S. Kim and S. Nam, "Wideband and low-profile array of tightly coupled dipole subarrays," *Journal of Electromagnetic Engineering and Science*, vol. 24, no. 5, pp. 541–543, 2024.

[16] T. Yoon, U. Park, and J. Oh, "Band-stop behavior vertically extended ground isolator based on transmission line theory for ibfd trx decoupling applications," *IEEE Transactions on Microwave Theory and Techniques*, vol. 72, no. 2, pp. 1405–1415, 2023.

[17] N. BniLam, J. Steckel, and M. Weyn, "Synchronization of multiple independent subarray antennas: An application for angle of arrival estimation," *IEEE Transactions on Antennas and Propagation*, vol. 67, no. 2, pp. 1223–1232, 2018.
[18] J. Kim, W. Lee, and J. Oh, "Liquid-crystal-tuned resonant series patch array with unique element spacing emulating simplified operating construe of traveling-wave antenna," *IEEE Antennas and Wireless Propagation Letters*, vol. 22, no. 12, pp. 3087–3091, 2023.
[19] H. Kim, *et al.*, "Low-power consumption and beam-sustainable reconfigurable intelligent surface for fixed wireless communication at millimeter-wave 5g band," *IEEE Transactions on Microwave Theory and Techniques*, pp. 1–12, 2025.
[20] S. Wang, Z. Li, M. Chen, and J. Wang, "Electronically controlled fixed-frequency beam-scanning periodic leaky-wave antenna with positive-order-harmonic radiations," *IEEE Antennas and Wireless Propagation Letters*, vol. 21, no. 8, pp. 1610–1614, 2022.
[21] S. Wang, Z. Li, and J. Wang, "A quad-polarization reconfigurable fixed-frequency beam-scanning leaky-wave antenna based on the holographic method for millimeter-wave application," *IEEE Transactions on Antennas and Propagation*, vol. 71, no. 1, pp. 723–733, 2022.
[22] M. Boyarsky, T. Sleasman, M. F. Imani, J. N. Gollub, and D. R. Smith, "Electronically steered metasurface antenna," *Scientific Reports*, vol. 11, no. 1, p. 4693, 2021.
[23] S. Ali, H. M. Cheema, and F. A. Ghaffar, "Beam steerable half mode SIW leaky-wave antenna using FPMS," *IEEE Journal of Microwaves*, vol. 3, no. 4, pp. 1187–1198, 2023.
[24] H. Kim, S. Oh, S. Bang, H. Yang, B. Kim, and J. Oh, "Independently polarization manipulable liquid-crystal-based reflective metasurface for 5G reflectarray and reconfigurable intelligent surface," *IEEE Transactions on Antennas and Propagation*, vol. 71, no. 8, pp. 6606–6616, 2023.
[25] H. Kim, *et al.*, "Low voltage controlled fast switchable liquid crystal-based reflectarray with transverse rubbing layer," *IEEE Antennas and Wireless Propagation Letters*, 2024.
[26] S. Bang, H. Kim, and J. Oh, "Enhancing 2-D beam scanning capability through extended transmission paths in a liquid crystal-based transmitarray antenna for mmWave communications," *Journal of Electromagnetic Engineering and Science*, vol. 25, no. 1, pp. 85–91, 2025.
[27] J. Kim, J. Kim, J. H. Oh, S.-H. Wi, and J. Oh, "Rotated feed-combined reconfigurable transmit RIS with disparate deployment of 1-bit hybrid units for B5G/6G," *IEEE Transactions on Antennas and Propagation*, vol. 71, no. 6, pp. 5457–5462, 2023.
[28] B. Moon, S. Bang, H. Kim, and J. Oh, "Simultaneously dual-polarization convertible sub-THz reconfigurable intelligent surface enabled by through-quartz vias," in *2024 18th European Conference on Antennas and Propagation (EuCAP)*. IEEE, 2024, pp. 1–5.
[29] H. Kim, B. Moon, S. Bang, S. Oh, and J. Oh, "PCB-based dual-polarized liquid crystal reflectarray with high aperture efficiency and bridge-shaped biasing topology for 2D scanning," *IEEE Access*, 2025.
[30] B. Moon, S. Bang, S. Oh, and J. Oh, "Design and experimental validation of a through-quartz via-based LC RIS for dual-polarization beam steering in sub-terahertz bands," *IEEE Open Journal of Antennas and Propagation*, 2025.
[31] S. N. M. Zainarry, N. Nguyen-Trong, and C. Fumeaux, "A frequency- and pattern-reconfigurable two-element array antenna," *IEEE Antennas and Wireless Propagation Letters*, vol. 17, no. 4, pp. 617–620, 2018.
[32] L. Nov, T. Chrek, and J.-Y. Chung, "Characterization of resistance and inductance of PIN diode at mmWave frequency using 7-layer deep neural network," *IEEE Access*, vol. 11, pp. 126 782–126 790, 2023.
[33] D. Yang and S. Nam, "Frequency reconfigurable beam scanning squarely modulated reactance surface antenna with period and surface reactance control," *IEEE Access*, vol. 11, pp. 72 552–72 561, 2023.
[34] M. Frank, R. Weigel, and A. Koelpin, "Design of a 24 GHz reconfigurable transmitarray element with continuous phase range," in *2017 11th European Conference on Antennas and Propagation (EuCAP)*. IEEE, 2017, pp. 2400–2404.
[35] Y. Zhu, *et al.*, "Millimeter-wave reconfigurable intelligent surface with independent and continuous amplitude-phase control: Unit cell design and circuit model," *IEEE Transactions on Antennas and Propagation*, 2025.
[36] U. Park, T. Yoon, and J. Oh, "A compact active bidirectional phase shifter employing a highly isolated single gilbert cell," *IEEE Microwave and Wireless Technology Letters*, pp. 1–4, 2025.
[37] U. Park, S. Hwangbo, J. Kim, T. Yoon, and J. Oh, "A novel switch-less active bi-directional phase shifter with in–out impedance equalization via staggered structure for ku-band applications," *IEEE Transactions on Microwave Theory and Techniques*, vol. 73, no. 5, pp. 2653–2667, 2025.

Seungwoo Bang (Graduate Student Member, IEEE) received the B.S. degree from Seoul National University of Science and Technology, South Korea, in 2022. He is currently pursuing the integrated master's and Ph.D. degrees with the Department of Electrical and Computer Engineering at Seoul National University, South Korea. His current research interests include metasurface and antenna design.

Jaehoon Kim (Member, IEEE) received the B.S. degree in electronic and electrical engineering from Sungkyunkwan University, Suwon, South Korea, in 2018, and the Ph.D. degree in electrical and computer engineering from Seoul National University, Seoul, South Korea, in 2025. He is currently a Staff Engineer with the Core Component Technology Team, MX Business, Samsung Electronics, Suwon, South Korea. His current research interests include RF systems, with an emphasis on handset antenna radiation system design. His doctoral research focused on reconfigurable antennas, metasurfaces, and reconfigurable intelligent surfaces for next-generation wireless communications.

Jungi Jeong (Member, IEEE) received the B.S. degree in Electronic Engineering from Kwangwoon University, Seoul, Korea, in 2013, and the Ph.D. degree in Electrical and Electronic Engineering from Yonsei University, Seoul, Korea, in 2019. From September 2019 to July 2020, he worked in the Network Division of Samsung Electronics, and developed antennas for 5G base stations. He currently works in the 6G research team at Samsung Research, Seoul, Korea, and serves as an RF/Antenna Engineer investigating B5G/6G communications. His research interests include millimeter/THz wave antennas, metamaterials, metasurfaces, lenses, reflectarrays, wave propagation, and antenna measurement. He received the Minister Prize from the Ministry of Science and ICT, Korea, in 2018.

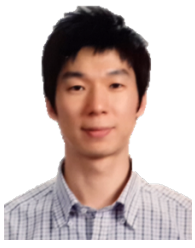

Junhwa Oh (Member, IEEE) received his B.S. and M.S. degrees in Electric and Electronic Engineering from Yonsei University, Seoul, Korea, in 2007 and 2009, respectively. In 2009, he joined Samsung Electronics as an Antenna Engineer. He worked in the Mobile-eXperience (MX) division for 10 years and developed mobile phone antennas for 2G/3G/4G/5G communications and WiFi, Bluetooth, and GPS connectivity. Since 2019, he has worked as a principal engineer in the 6G research team at Samsung Research, Seoul, Korea. He is currently developing advanced antenna and metamaterial technologies for B5G/6G communication systems. His research interests include electromagnetic wave propagation, antenna design and measurement, reconfigurable antennas, microwave/RF circuits, and computational electromagnetics.

Byeongjin Kim (Graduate Student Member, IEEE) received a B.S. degree in electrical and computer engineering from Seoul National University, Korea, in 2020, where he is currently pursuing the integrated master's and Ph.D. degree. His current research interests include display antenna and antenna-inpackage for smartphone, transparent antenna, passive and active transmitarray and reflectarray, and metasurface antenna for 5G millimeter-wave communication systems.

Jungsuek Oh (S'08) received his B.S. and M.S. degrees from Seoul National University, Korea, in 2002 and 2007, respectively, and a Ph.D. degree from the University of Michigan at Ann Arbor in 2012. From 2007 to 2008, he was with Korea Telecom as a hardware research engineer, working on the development of flexible RF devices. In 2012, he was a postdoctoral research fellow in the Radiation Laboratory at the University of Michigan. From 2013 to 2014, he was a staff RF engineer with Samsung Research America, Dallas, working as a project leader for the 5G/millimeter-wave antenna system. From 2015 to 2018, he was a faculty member in the Department of Electronic Engineering at Inha University in South Korea. He is currently an Associate Professor in the School of Electrical and Computer Engineering, Seoul National University, South Korea. His research areas include mmWave beam focusing/shaping techniques, antenna miniaturization for integrated systems, and radio propagation modeling for indoor scenarios. He is the recipient of the 2011 Rackham Predoctoral Fellowship Award at the University of Michigan. He has published more than 50 technical journal and conference papers, and has served as a technical reviewer for the IEEE Transactions on Antennas and Propagation, IEEE Antenna and Wireless Propagation Letters, and so on. He has served as a TPC member and as a session chair for the IEEE AP-S/USNC-URSI and ISAP. He has been a senior member of IEEE since 2017.